Transonic Drag Reduction Through Trailing-Edge Blowing on the FAST-MAC Circulation Control Model

David T. Chan*, Gregory S. Jones, William E. Milholen, II[‡], and Scott L. Goodliff[§]

NASA Langley Research Center, Hampton, VA, 23681

A third wind tunnel test of the FAST-MAC circulation control semispan model was completed in the National Transonic Facility at the NASA Langley Research Center where the model was configured for transonic testing of the cruise configuration with 0° flap deflection to determine the potential for transonic drag reduction with the circulation control blowing. The model allowed independent control of four circulation control plenums producing a high momentum jet from a blowing slot near the wing trailing edge that was directed over a 15% chord simple-hinged flap. Recent upgrades to transonic semispan flow control testing at the NTF have demonstrated an improvement to overall data repeatability, particularly for the drag measurement, that allows for increased confidence in the data results. The static thrust generated by the blowing slot was removed from the wind-on data using force and moment balance data from wind-off thrust tares. This paper discusses the impact of the trailing-edge blowing to the transonic aerodynamics of the FAST-MAC model in the cruise configuration, where at flight Reynolds numbers, the thrust-removed corrected data showed that an overall drag reduction and increased aerodynamic efficiency was realized as a consequence of the blowing.

Nomenclature

Symbols		$C_{\scriptscriptstyle dis}$	Nozzle discharge coefficient
		F_{mom}	Momentum thrust, lbf
AF	Axial Force, lbf	g	Standard gravitational acceleration
\mathcal{R}	Aspect ratio	3	$(=32.174 \text{ ft/sec}^2)$
b	Wing span, in	h	Blowing slot height, in
c	Local wing chord, in	M_{∞}	Freestream Mach number
\overline{c}	Mean aerodynamic chord, in	$N\widetilde{F}$	Normal force, lbf
$C_{\scriptscriptstyle A}$	Axial force coefficient, body axis	NPR	Nozzle pressure ratio, (p_a/p_{∞})
$C_{\scriptscriptstyle D}$	Drag coefficient, stability axis	$NPR_{\scriptscriptstyle critical}$	Critical nozzle pressure ratio for
$C_{\scriptscriptstyle L}$	Lift coefficient, stability axis	criticai	sonic condition (=1.893 for γ =1.4)
C_{ι}	Rolling moment coefficient, body axis	NPR_{exit}	Nozzle exit pressure ratio, (p_o/p_{exit})
C_m	Pitching moment coefficient, body	$p_{_{\infty}}$	Freestream static pressure, psi
	axis	$p_{_{b}}$	Ambient back pressure, psi
$C_{\scriptscriptstyle N}$	Normal force coefficient, body axis	p_{exit}	Slot exit static pressure, psi
C_n	Yawing moment coefficient, body	p_o	Stagnation pressure, psi
	axis	p_{t}	Tunnel stagnation pressure, psi
C_p	Pressure coefficient	$\stackrel{\iota}{P}M$	Pitching moment, in-lbf
$\hat{C_n^*}$	Critical pressure coefficient	$q_{_{\infty}}$	Freestream dynamic pressure, psf
$\stackrel{r}{\stackrel{r}{C_Y}}$	Side force coefficient, body axis	$\overset{\scriptscriptstyle{1}_{\infty}}{Re}$	Reynolds number based on mean
C	Momentum thrust coefficient	-	V

^{*}Research Aerospace Engineer. Configuration Aerodynamics Branch. Member AIAA. david.t.chan@nasa.gov

 $^{^{\}dagger}$ Research Aerospace Engineer. Configuration Aerodynamics Branch. Associate Fellow AIAA. gregory.s.jones@nasa.gov

 $^{^\}ddagger$ Research Aerospace Engineer. Configuration Aerodynamics Branch. Senior Member AIAA. william.e.milholen@nasa.gov

[§]Test Engineer. Jacobs Technology, Inc. Member AIAA. scott.l.goodliff@nasa.gov

	aerodynamic chord	ft	feet
RM	Rolling Moment, in-lbf	in	inches
S_{ref}	Wing reference area, ft ²	lbf	pounds force
SF	Side Force, lbf	$_{ m lbm}$	pounds mass
T_o	Stagnation temperature, °R	${ m M}$	million, 1×10^6
T_{t}	Tunnel stagnation temperature, °F	psf	pounds per square foot
U	Local velocity, ft/sec	psi	pounds per square inch
\dot{w}	Weight flow rate, lbm/sec		
α, AOA	Angle of attack, deg	Acronyms	
Δ	denotes increment or difference	BCRS	Balance Cavity Recirculation System
η	Semispan location	BMC	Balance Moment Center
γ	Ratio of specific heats (=1.4 for dry	CFD	Computational Fluid Dynamics
	air)	EU	Engineering Units
ψ	Yaw angle, deg	F&M	Force & Moment
$\psi_{\scriptscriptstyle thrust}$	Blowing jet thrust yaw angle, deg	FAST-MAC	Fundamental Aerodynamics
ho	Density, lbm/ft ³		Subsonic/Transonic-Modular Active
θ	Pitch angle, deg		Control
$\theta_{\scriptscriptstyle thrust}$	Blowing jet thrust pitch angle, deg	FS	Full-Scale
Subscripts		HPA	High Pressure Air
	Freestream quantity	LaRC	Langley Research Center
∞ bal	Balance measurement	MCV	Multiple Critical Venturi
exit	Slot exit location	MRC	Moment Reference Center
jet	Jet quantity	NASA	National Aeronautics and Space
TR	Thrust-removed quantity		Administration
	Till dot Tellio ved qualities	NTF	National Transonic Facility
Units		OML	Outer Mold Line
$^{\circ}$, deg	degrees	PIP	Pressure Interface Piece
$^{\circ}\mathrm{F}$	degrees Fahrenheit	SMSS	Sidewall Model Support System
cts	counts (0.0001)	WT	Wind Tunnel

foot

I. Introduction

Many of the advanced future aircraft being designed today utilize advanced propulsion and active flow control systems that closely integrate the engine and airframe. Cruise efficiency, community noise, and runway independence can no longer be optimized independently because of the close coupling of the engine, airframe, and wing. Circulation control techniques have experienced a resurgence recently, with many research efforts focusing on developing databases for CFD validation, as unreliable predictions have been a barrier to applying the techniques to aircraft. The lack of Reynolds number scaling data is also a shortfall of many active flow control datasets.

Evaluating the benefits of active flow control systems on scaled wind tunnel models requires added attention to detail. Not only does the outer mold line of the model need to accurately represent the proposed flight vehicle, but also the intricate details of the flow control system. Additionally, if the flow control system adds a net thrust to the flow field, it is necessary to accurately characterize the static thrust produced in order to remove its effect and isolate the induced aerodynamic effects of the flow control system. It is also desirable that the wind tunnel testing be conducted at Reynolds numbers that are representative of flight conditions, to document the appropriate scaling parameters, and ensure the active flow control technique is properly scaled to the flight vehicle.

aanadrmamia ahand

The circulation control method that is discussed throughout the paper is one where a high momentum jet from a blowing slot near the wing trailing edge is tangentially ejected over the curved surface

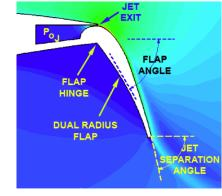


Figure 1. Circulation control blowing example.

of a simple short-chord hinged flap (Figure 1). The Coandă effect causes the jet to remain attached to the

curved surface because of a balance between the low static pressures in the jet sheet and the centrifugal force around the curvature of the surface. Let $^{14,\,15}$ For circulation control applications, the jet flow is typically characterized at the exit of the blowing slot by the nondimensional jet momentum coefficient C_{μ} . The nondimensional slot height (h/c), the plenum stagnation conditions $(p_o)_{jet}, (T_o)_{jet}$, and the weight flow rate (w_{jet}) are the key measurements to be made to quantify C_{μ} . In addition, the slot exit static pressure (p_{exit}) is needed to complete the calculation of the total thrust produced at the slot exit.

A third active flow control experiment (Test 222) was recently conducted in the National Transonic Facility (NTF), shown in Figure 2(a), at the NASA Langley Research Center (LaRC). The Fundamental Aerodynamics Subsonic/Transonic-Modular Active Control (FAST-MAC) model was again used to test circulation control concepts at realistic flight Reynolds numbers at transonic cruise conditions, building upon the successes and lessons learned of the first two test entries (NTF Tests 195 and 213). The FAST-MAC model has a super-critical wing and represents an advanced configuration that is characteristic of modern aircraft. The geometry and results of the high Reynolds number tests in the NTF can be openly distributed to the research community to aid in CFD validation. The model is also unique in that it integrates circulation control strategies to be evaluated at transonic Mach numbers, where little research has been published except on two-dimensional airfoils. Figure 2(b) shows a photograph of the FAST-MAC model installed in the NTF test section.



(a) Aerial view of the NTF.



(b) FAST-MAC model in cruise configuration in the NTF

Figure 2. National Transonic Facility and FAST-MAC model.

In this third test entry, the model was tested at transonic Mach numbers at 15 million and 30 million chord Reynolds numbers to investigate the effect of the trailing-edge blowing on the transonic aerodynamics. The test was also an opportunity to evaluate multiple system improvements for transonic semispan active flow control testing at the NTF and its effect on data quality. The upgrades that were implemented have resulted in even further improvements to data quality and repeatability, particularly in the transonic speed range, building upon the improvements demonstrated in the second test entry.

Previous analysis of the wing surface pressures revealed that for attached flow conditions at $M_{\infty}=0.85$, the circulation control blowing increased the lift and moved the shockwave aft on the wing, without changing the strength of the shockwave.¹⁹ At the off-design conditions at $M_{\infty}=0.88$, the blowing was effective in reattaching the shock-induced flow separation, moving the shockwave aft approximately 5% chord with no increase in shockwave strength. These encouraging results suggest that the circulation control blowing was effective in reducing the transonic drag on the configuration, however, this cannot be quantified until the thrust generated by the blowing slot is correctly removed from the force and moment balance data. The recent improvements to the semispan force measurement system at the NTF has provided confidence that the balance data from wind-off static thrust tares can be used to remove the effect of the static thrust.

This paper discusses the induced effects of the trailing-edge blowing on the transonic aerodynamics of the FAST-MAC model. The results will be focused on Mach numbers of 0.85 and 0.88 at Reynolds numbers based on the mean aerodynamic chord of 15 million and 30 million. Two methods for static thrust removal are evaluated and the results are compared against each other. The lift, drag, and aerodynamic efficiency increments due to the induced effects of the blowing slot are quantified for the cruise configuration using the thrust-removed force and moment balance data. The increment data are presented with uncertainty bounds to assess the quality of the increments, and an uncertainty quantification discussion is also presented to justify the uncertainty bounds attached to the data.

II. Wind Tunnel Description

The NTF^{20,21} is one of a limited number of wind tunnel facilities that can achieve flight Reynolds numbers and Mach numbers for subsonic transport type aircraft for both cruise and high-lift operations.²² The tunnel is a fan-driven, closed-circuit, continuous-flow, pressurized wind tunnel capable of operating either in dry air at warm temperatures up to 120°F or in nitrogen gas from warm to cryogenic temperatures down to -270°F. The wind tunnel is capable of an absolute pressure range from 1 to 9 atmospheres, a Mach number range from 0.1 to 1.2, and a maximum unit Reynolds number of 146x10⁶ per foot. Figure 3 shows the major components of the NTF

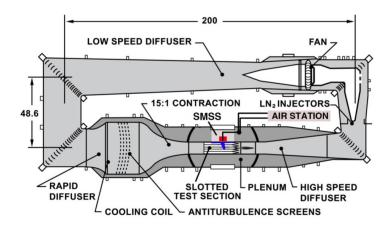


Figure 3. Major components of the NTF tunnel circuit including the SMSS and Air Station (linear dimensions in feet).

tunnel circuit, including the location of the sidewall model support system (SMSS) used for semispan model testing and the location of the high pressure air (HPA) delivery station needed for propulsion simulation and flow control experiments. The HPA station has two multiple critical venturi (MCV) systems to measure the total weight flow rate through the system. The NTF test section is 8.2 feet by 8.2 feet in cross section and 25 feet in length. The test section floor and ceiling are slotted (6 percent open), and the sidewalls are solid.

A. Transonic Semispan Testing

In the NTF, semispan models are installed on the tunnel sidewall and are attached to the external Force Measurement System (FMS) inside the SMSS, which houses the large NTF-117S force and moment (F&M) strain gauge balance. For flow control or propulsion experiments, the Pressure Interface Piece (PIP) is used to transfer the incoming HPA across the nonmetric / metric boundary of the F&M balance. A nonmetric standoff is used to offset the model from the tunnel sidewall and the metric break is preserved through the use of a labyrinth seal. The challenge in this type of testing is that the balance is designed to operate at 100°F while the tunnel can operate at cryogenic temperatures such as -50°F, as shown in Figure 4. Large pressure gradients established by the aerodynamics of the test article can cause both cold air from the tunnel

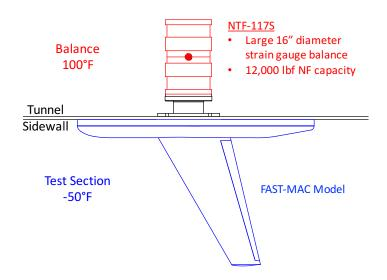


Figure 4. Simplified representation of the FAST-MAC semispan model installed to the NTF external force measurement system. Note the temperature difference between the test section and balance.

test section to be ingested into the balance cavity and heated air to be pulled out from the SMSS into the test section, through the gap in the model labyrinth seal. For data quality, the balance temperatures must remain stable with minimal temperature gradients across the balance. The SMSS provides a heated enclosure that maintains a stable temperature for the balance and the pitch mechanisms through the use of convective heat transfer provided by the closed loop Balance Cavity Recirculation System (BCRS). As shown in Figure 5, the BCRS constantly circulates heated air throughout the balance cavity and around the balance to counteract the cold air flow ingestion from the tunnel test section.

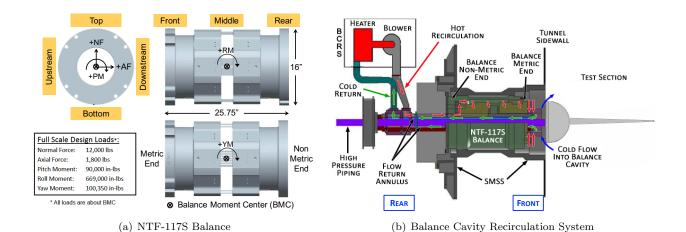


Figure 5. NTF-117S strain gauge balance and Balance Cavity Recirculation System used for semispan testing at the NTF.

B. Data Quality Improvements

The FAST-MAC experiments were some of the first uses of the transonic semispan test capability at NTF, but they exposed shortcomings in the capability, specifically in data quality and data repeatability. The levels of data repeatability from those tests were unacceptable for assessing cruise performance of the configurations and made it difficult to trust some of the test results. The major sources of the problem were determined to be a nonrepeatable load path in the SMSS FMS and thermal instability of the F&M balance during cryogenic tunnel operations.

Upgrades and improvements to the SMSS FMS were completed in recent years to fix these problems resulting in positive effects on data quality and data repeatability.^{23,24} The load path was improved with the addition of a mounting adapter that was installed to the front of the balance and kept the air delivery pipes secured in place and eliminated the instrumentation tube

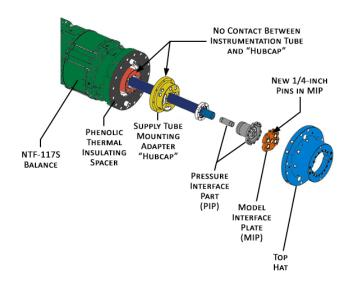


Figure 6. SMSS Force Measurement System arrangement and assembly. $\,$

from affecting the load path. Furthermore, two pins were added to the model interface plate to ensure a repeatable installation. These improvements are shown in Figure 6 and have contributed to very repeatable wind-off zero loads during semispan tests.

The thermal stability of the F&M balance was improved through a series of upgrades to the BCRS. The existing instrumentation tube was replaced with a larger diameter carbon-fiber tube, which increased the annular area for the BCRS flow path and thereby increased the allowable flow rate. Additionally, the BCRS blower motor and heater wiring were upgraded to allow the BCRS to provide more heat at higher flow rates. Finally, the BCRS control system was improved to provide better and quicker adjustments to changing tunnel operating conditions and prevent temperature gradients from forming across the balance. Other minor improvements such as sealing small gaps and holes in the back of the SMSS and in the model have also contributed to better temperature stability.

Other modifications^{25,26} at the NTF have focused on improving overall data quality and data repeatability. Several data processing techniques explored during these studies were determined to significantly improve data repeatability and are now part of the standard data reduction process at the facility. Acquiring longer duration data points to increase the number of samples in a data point decreased the scatter seen in the averaged data values. These longer data points also allow the use of conditional data sampling, where

only samples that are within a specified Mach number tolerance are used in the averaged data values. The conditional sampling technique requires that the data samples are time-aligned properly so that instrumentation time lags are taken into account, and that there are enough data samples within tolerance to create a proper averaged data value. The technique has been shown to significantly improve transonic drag data repeatability $(M_{\infty} \geq 0.8)$ due to the high correlation between Mach number and aerodynamic drag at those Mach numbers.

The result of the system upgrades, improvements, and lessons learned is shown in Figure 7 as each successive test entry of the FAST-MAC circulation control model in the NTF has demonstrated improved drag data repeatability from the previous entry. The ultimate goal is to improve the data repeatability of the drag coefficient C_D for subsonic transport models at transonic speeds to within one drag count ($C_D \pm 0.0001$) for semispan models.

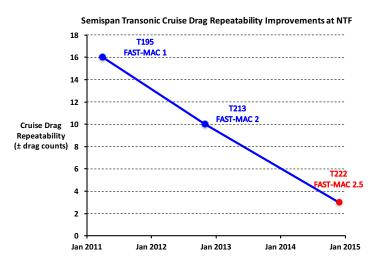


Figure 7. Improvement in transonic drag data repeatability through FAST-MAC test entries in the NTF.

III. Experimental Setup

A. Test Article

The FAST-MAC model shown in Figure 8 has a modern super-critical wing and was designed to become an NTF standard for evaluating performance characteristics of integrated active flow control and propulsion systems. The outer mold line (OML) of the model was designed for a cruise Mach number of 0.85 and a lift coefficient of 0.50, at a Reynolds number based on mean aerodynamic chord of 30×10^6 . A tangential blowing slot is located at the 85% chord location on the upper surface, and is directed over a 15% chord simple hinged flap for both the cruise and high-lift configurations. The wing is mounted in the mid-fuselage position and has an aspect ratio of 5.28, a leading edge sweep of 30°, a semispan of 48.0 inches, a mean aerodynamic chord of 19.4 inches, and a reference area of 6.06 ft². Even though the wing has a moderate aspect ratio, it represents the state-of-the-art in transonic super-critical wing design.^{27,28} The model is offset from the tunnel sidewall using a 2.0-inch nonmetric standoff,²⁹ which has a profile shape identical to that of the fuselage centerline.

The FAST-MAC model utilized four independent flow paths to achieve lift and thrust performance along the span of the circulation control flap as shown in Figure 9. Each plenum section had its own flow control valve located in the fuselage that fed a rapid diffuser located in the wing box. The diffuser is used to subdivide the incoming flow to the plenum, allowing it to be supplied at four evenly spaced spanwise locations. Each plenum had four perforated plates (17% open area) designed to maintain flow uniformity into the aft plenum settling chamber.³⁰ The flow then enters the aft plenum region of the model, where the upper plenum cover is supported by streamlined standoffs, which are used to set the blowing slot height. The aft section of the plenum had a 12-to-1 contraction ratio for the h/c = 0.0021 cruise configuration. For each configuration, care was given to accurately set and measure the slot exit areas for each plenum, as this plays an important role in computing the added thrust.

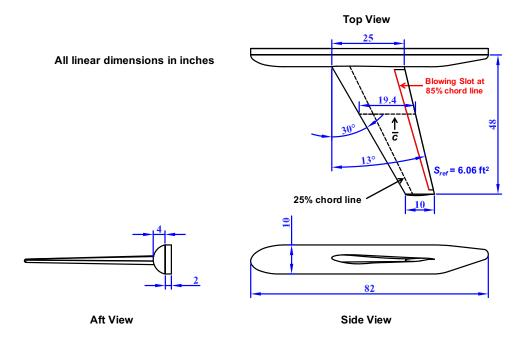


Figure 8. 3-view drawing with pertinent dimensions of the FAST-MAC semispan model in cruise configuration.

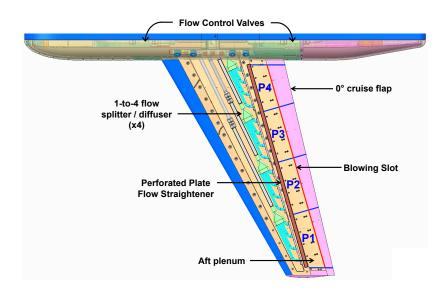


Figure 9. Four independent flow paths in the FAST-MAC model.

B. Experimental Measurements

1. Force and Moment Measurements

The NTF-117S³¹ balance shown earlier in Figure 5(a) is a large five-component (no side force measurement capability) strain gauge balance that is mounted inside the SMSS and is the primary FMS for semispan models in the NTF. The balance is 16 inches in diameter and about 26 inches in length and has resistance temperature detector (RTD) sensors all around the balance to be able to monitor temperature gradients that may develop from the front-to-rear, top-to-bottom, and upstream-to-downstream directions. The Pressure Interface Piece (PIP) allows the high-pressure supply air needed for propulsion and flow control simulation testing to "bridge" the balance by crossing from the nonmetric end to the metric end. Consequently, the balance and PIP must be considered together as a system and calibrated accordingly. Table 1 shows the design loads of the balance and the results of the system calibration.^{23, 24} The calibration accuracies are presented both as a percentage of full-scale load and in engineering units of lbf or in-lbf. The right side of the

table converts the numbers to aerodynamic coefficient accuracies at conditions for the FAST-MAC model.

Table 1. NTF-117S force measurement system calibration results (includes effect of PIP pressure and temperature).

		Calibration		Coefficient Accuracy for			
		A	Accuracy FAST-MAC Model				
Balance	Calibration			$M_{_{\infty}}=0.85$	$M_{\infty} = 0.85$	$M_{\infty} = 0.88$	$M_{\infty} = 0.88$
Component	Load Range	%-FS	EU	Re = 15M	Re = 30M	Re = 15M	Re = 30M
AF	$\pm 1,800 \text{ lbf}$	0.258	$\pm 4.64 \text{ lbf}$	± 0.0005	± 0.0004	± 0.0005	± 0.0004
NF	$\pm 12,000 \text{ lbf}$	0.207	$\pm 24.84 \text{ lbf}$	± 0.0026	± 0.0020	± 0.0025	± 0.0020
PM	$\pm 90,000$ in-lbf	0.367	± 330.30 in-lbf	± 0.0018	± 0.0014	± 0.0017	± 0.0014
RM	$\pm 670,000$ in-lbf	0.235	± 1574.5 in-lbf	± 0.0034	± 0.0027	± 0.0033	± 0.0027
YM	$\pm 110,000$ in-lbf	0.364	± 400.4 in-lbf	± 0.0009	± 0.0007	± 0.0008	± 0.0007

2. Internal Flow Path Measurements

The weight flow rate and thrust from the blowing slot are calculated assuming a one-dimensional isentropic expansion from measured stagnation conditions. In each plenum, there are two pitot probes to measure the stagnation pressure and two thermocouples on the probes to measure the stagnation temperature. The two measurements are averaged to produce the stagnation quantities to be used in the isentropic equations. Additionally, one surface pressure tap on the flap for each plenum is used to measure the slot exit static pressure. These are used to check the behavior of the slot exit and are used to calculate the pressure thrust component of the total thrust from the slot exit.

Figure 10(a) shows a planform view of the FAST-MAC model and the locations of the stagnation pressure and temperature measurements in each plenum and the static pressure measurements on the flap at the slot exit. Figure 10(b) shows a section cut normal to the slot at the flap pressure row for plenum #4 on the 0 degree cruise flap, as an example. The design intent was to locate one of the static pressure taps from each pressure row to be at the apex of the first flap radius that corresponds to the jet exit plane so that the pressure tap would be normal to the blowing jet. However, due to space limitations and machining uncertainty, some of the taps are not lined up exactly with the slot exit, which introduces uncertainty in these measurements.

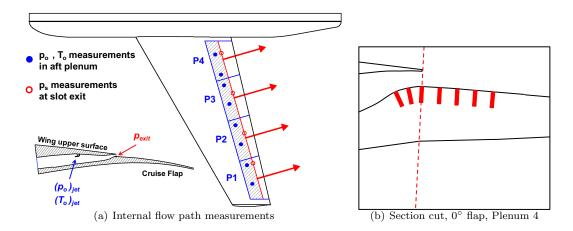


Figure 10. Locations of measured stagnation quantities and measured exit static pressure for each plenum. Section cut normal to the slot detailing the locations of the static pressure taps. Plenum #4 of the 0° flap (h/c = 0.0021) configuration shown as an example.

The classical definition of nozzle pressure ratio (NPR) is shown in Equation 1. The pressure ratio at the slot exit (NPR_{exit}) is shown in Equation 2 and is different than the classical definition of NPR due to influences of the wall-bounded jet. The value listed for $NPR_{critical}$ in Equation 3 represents the minimum pressure ratio for choked flow to occur for $\gamma=1.4$. These quantities form the basis for calculating the thrust from the blowing slot and the scaling parameter C_{μ} .

$$NPR = \frac{(p_o)_{jet}}{p_\infty} \qquad (1) \qquad NPR_{exit} = \frac{(p_o)_{jet}}{p_{exit}} \qquad (2) \qquad NPR_{critical} = 1.893 \qquad (3)$$

IV. Results

A. Data Repeatability

Throughout the test, planned repeat runs were performed in order to assess data repeatability. Since the focus of the test was on the cruise configuration, repeat runs were acquired at Mach numbers of 0.85 and 0.88 for chord Reynolds numbers of 15 and 30 million, at various NPR values in an angle-of-attack range between -6 and 6 degrees. These repeat runs were sometimes performed back-to-back to assess short term repeatability and sometimes they were performed at the end of a run set to assess longer term repeatability.

The methods used to analyze the data repeatability in the experiment are derived from analyses commonly used in Statistical Process Control (SPC).^{32,33} The Analysis of Normalized Ranges (ANOR) with mean ranges has been used frequently because of its simplicity and also because of its ability to handle varying numbers of data points within a group and varying numbers of groups within an experiment.

The process for modeling the variance of each set of repeat runs is listed below:

- 1. Interpolate each data set to nominal independent variable (e.g., α) values x_i , if necessary;
- 2. For the dependent variable of interest (e.g., C_D), calculate the mean of the y_i values at each x_i ;
- 3. Calculate the residuals from the mean for each y_i value;
- 4. Calculate the range of the y_i residuals $(R = \max \min)$ at each x_i ;
- 5. Normalize each individual range by the quantity d_2 to produce an individual dispersion quantity (R/d_2)

The SPC quantity d_2 relates the mean range for a normal distribution to its standard deviation and is a function of the sample size. The individual dispersion quantities from each set of repeat runs are pooled and the mean of these quantities are used to calculate an estimated standard deviation as shown in Equation 4.

$$\hat{\sigma} = \overline{R} / d_2 \tag{4}$$

An example of this process is shown in Figure 11 for the drag coefficient C_D at Mach 0.85 and 30 million Reynolds number at an NPR value of 1.5. The calculated standard deviation and range analysis levels are shown on the residual plot and in this particular example, the drag coefficient repeated to within ± 1.8 counts. For comparison, the balance system accuracy at this condition is ± 4 counts. This process was performed for all repeat run sets acquired during the test.

The individual dispersion quantities from each of the repeat run sets can be pooled together to estimate the total variation in the experiment if the variation is random. This is shown in Table 2 for several parameters of interest such as the drag coefficient and the aerodynamic efficiency parameter. As stated earlier and shown in Figure 7, the significant improvement in the repeatability of the drag coefficient provides confidence in the evaluation of wing trailing-edge blowing for vehicle transonic performance benefits.

Table 2. Summary of overall data repeatability levels for the FAST-MAC cruise configuration.

Parameter	2σ Data Repeatability		
C_D	± 0.00034		
C_L	± 0.0014		
C_m	± 0.0010		
M*L/D	± 0.104		

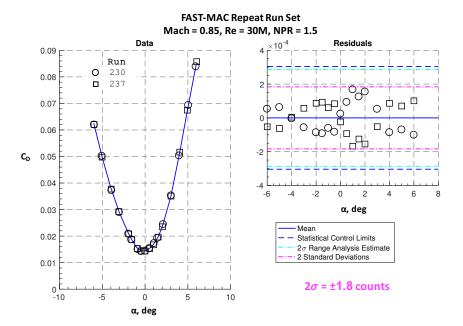


Figure 11. Example range analysis to assess C_D data repeatability at $M_{\infty}=0.85,\,NPR=1.5,$ and Re=30million.

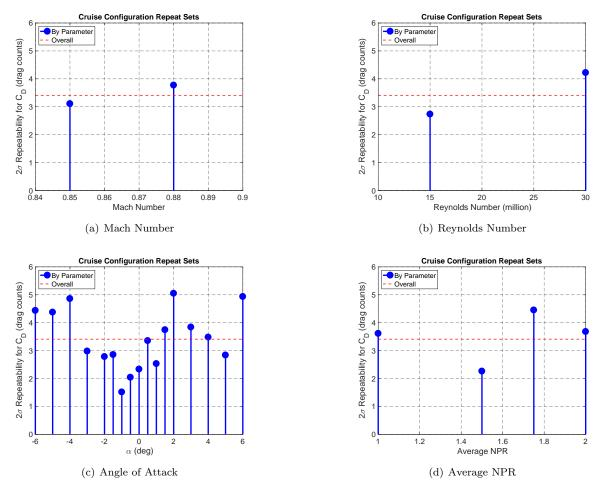


Figure 12. Trend of 2σ repeatability levels for C_D with (a) Mach number, (b) Reynolds number, (c) angle-of-attack, and (d) average NPR.

The individual dispersion quantities can also be pooled as a function of independent variables to determine whether the variation is physics-based and therefore, has a trend with an independent variable. These trends can sometimes help determine the source of data variability in the experiment. An example of this trend information is shown in Figure 12 for the repeatability of C_D as a function of Mach number, Reynolds number, angle of attack, and average NPR. The overall repeatability level is also shown for reference on the plots. The plots do not show significant trends with any independent parameter suggesting that the repeatability variation is mostly a random error source.

B. Static Thrust Removal

In order to investigate possible transonic performance benefits due to wing trailing-edge blowing on the FAST-MAC model, the effect of the blowing jet static thrust needs to be removed from the wind-on balance measurements to isolate the pure aerodynamic and jet-induced effects in the force and moment data. This is accomplished by using the data from a wind-off static thrust tare. During a thrust tare run for the FAST-MAC model with the tunnel fan not operating ($M_{\infty}=0$), the four model valves are opened individually to set the NPR of each plenum to the desired level to ensure all plenums are flowing at the same NPR level. The temperatures in the plenums are allowed to come to equilibrium and then a data point is acquired. This process is repeated for all desired NPR levels up to the maximum NPR level achievable before model safety limits are reached.

For the FAST-MAC model, there are two methods that can be used for static thrust removal that will be presented in the following sections. The preferred method uses the balance measured forces and moments from a wind-off static thrust tare to determine the components of the static thrust. Alternatively, the measured stagnation quantities in each plenum can be used to calculate the ideal thrust from the blowing slot assuming a one-dimensional isentropic expansion, then the resultant thrust can be resolved along the x, y, and z directions using the geometric thrust vector angles.

Each of the two thrust removal methods has limitations that can increase the uncertainty in the thrust removal process. The scatter or variation associated with the balance measurements could increase the uncertainty of the wind-off thrust tare data especially since the forces and moments generated during a thrust tare are at the low end of the balance measurement capability. For the ideal thrust method, there are many assumptions such as assuming the blowing slot operates like an axisymmetric convergent nozzle and that the flow from the blowing slot is uniform across the span of the wing. Furthermore, geometric variations in slot exit height and thrust vector angles introduce additional uncertainty into the results.

1. Using Balance Force and Moment Data

The balance force and moment measurements acquired during wind-off static thrust tares describe the effect of the static thrust as a function of NPR. Note that for the FAST-MAC model, the blowing slot is directed over the flap, therefore, the balance cannot distinguish between the pure static thrust effect (free-jet) and the aerodynamic Coandă effect of the wall-bounded jet and would instead measure the combined effect. The balance measurements can be used to determine the total resultant thrust magnitude, the resultant in the aircraft pitch axis, and the resultant in the aircraft yaw axis as shown in Equations 5, 6, and 7, respectively. The balance measurements can also be used to calculate the effective static thrust vector angles in the aircraft pitch and yaw axes as shown in Equations 8 and 9, respectively.

$$(F_R)_{bal}|_{total} = \sqrt{AF_{bal}^2 + NF_{bal}^2 + SF_{bal}^2}$$
 (5)

$$(F_R)_{bal}|_{pitch} = \sqrt{AF_{bal}^2 + NF_{bal}^2}$$
 (6)

$$(F_R)_{bal}|_{yaw} = \sqrt{AF_{bal}^2 + SF_{bal}^2}$$
 (7)

$$\theta_{thrust} = \tan^{-1} \left(\frac{-NF_{bal}}{AF_{bal}} \right) \tag{8}$$

$$\psi_{thrust} = \tan^{-1} \left(\frac{-SF_{bal}}{AF_{bal}} \right) \tag{9}$$

The measured thrust quantities are nondimensionalized since different back pressures usually exist between the wind-off conditions and the wind-on conditions. The desire is to remove the amount of static thrust that would have been present at the back pressure of the wind-on measurements. The " p_b method" involves dividing the static thrust quantities by the ambient back pressure from the static thrust tare and a reference area, where the reference area can be the nozzle throat or exit area or even the wing reference area. This is converted back to dimensional form in the thrust removal process by multiplying by the chosen reference area and the freestream static pressure (p_{∞}) of the wind-on data. The " p_b method" is usually used because it is simpler and produces mostly linear curves as a function of NPR.

2. Using Calculated Ideal Thrust

For flow control applications, one of the most important scaling parameters is the jet momentum coefficient (C_{μ}) , which requires the calculation of the jet momentum thrust. In each of the plenums in the FAST-MAC model, the plenum area contracts to the slot exit area by a 12-to-1 ratio for the cruise flap configuration, therefore for simplicity in the calculation of the blowing jet thrust, the blowing slot is assumed to operate like a two-dimensional axisymmetric convergent nozzle (Figure 13). Using the measured stagnation pressure and temperature inside the plenum just upstream of the slot exit as shown in Figure 14, isentropic equations for an ideal gas are used to calculate the thrust out of each plenum as the jet is assumed to expand adiabatically to the freestream static pressure. The thrust is calculated at the slot exit plane, which is normal to the wing upper surface by design. These equations ignore any internal boundary layer growth and pressure losses in the flowpath. It is also recognized that the blowing slot is not an axisymmetric nozzle and the actual wall-bounded jet can violate this assumption and introduce errors into the thrust and C_{μ} calculations.

Using the measured NPR in each plenum, various ideal jet quantities can be calculated for the blowing jet such as the velocity (U_{jet}) , Mach number (M_{jet}) , density (ρ_{jet}) , and weight flow rate $((\dot{w}_{jet})_{ideal})$ as documented in Reference 34. The Multiple Critical Venturi (MCV) system in the NTF air station provides a measure of the total weight flow rate

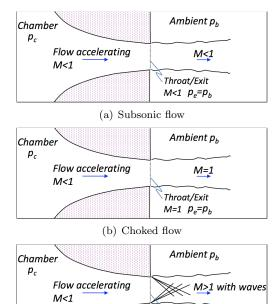


Figure 13. Operation of a convergent nozzle at a constant ambient back pressure.

(c) Choked flow, underexpanded

Throat/Exit M=1 p_e>p_b

through the model. The nozzle discharge coefficient $((C_{dis})_{jet})$ is calculated as the ratio of the measured weight flow rate to the ideal weight flow rate. The momentum thrust from the blowing slot is then calculated using the weight flow rate and the jet velocity at the slot exit as shown in Equation 10. The momentum thrust is nondimensionalized by the freestream dynamic pressure and wing reference area to produce the momentum thrust coefficient (C_{μ}) as shown in Equation 11. Finally, the momentum and pressure components of the blowing jet static thrust are added together to produce the resultant total thrust.

$$[(F_{mom})_{jet}]_{ideal} = \frac{(C_{dis})_{jet} (\dot{w}_{jet})_{ideal} U_{jet}}{g}$$
(10)

$$\left[\left(C_{\mu} \right)_{jet} \right]_{ideal} = \frac{\left[\left(F_{mom} \right)_{jet} \right]_{ideal}}{q_{\infty} S_{ref}} \tag{11}$$

The resultant total thrust can then be resolved along the x, y, and z directions using the geometric thrust vector pitch angle θ_{thrust} and yaw angle ψ_{thrust} as listed in Table 3. This is accomplished by performing pitch and yaw Euler rotations as shown in Equation 12. Note that the negative signs are the result of mapping the standard right-hand Euler axes to the aircraft body axes definition. To determine the moments generated at the moment reference center (MRC) due to the static thrust, the total thrust from each plenum is assumed to act at the center of each plenum span and the distances from the thrust vectors to the MRC are used. Finally, these forces and moments due to the blowing jet static thrust are nondimensionalized using the " p_b

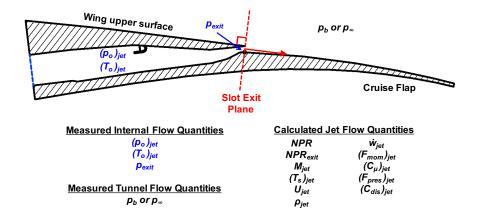


Figure 14. Calculation of static thrust and other internal flow quantities at slot exit plane using measured internal flow quantities for each plenum.

method" similar to the process with the balance measurements. This methodology for thrust removal using the calculated ideal thrust was also presented in Reference 34.

Table 3. Geometric thrust vector angles in the aircraft body axes.

Plenum	$\theta_{\scriptscriptstyle thrust}$	$\psi_{\scriptscriptstyle thrust}$
1	7.1°	-16.1°
2	7.2°	-16.1°
3	7.7°	-16.1°
4	8.0°	-16.1°

$$(F_{total})_x = F_{total} \cos \theta_{thrust} \cos \psi_{thrust}$$
(12a)

$$(F_{total})_y = -F_{total}\cos\theta_{thrust}\sin\psi_{thrust}$$
 (12b)

$$(F_{total})_z = -F_{total}\sin\theta_{thrust} \tag{12c}$$

3. Static Thrust Tare Results

The improvements in the overall force measurement system at the NTF provided confidence in the balance measurements and the static thrust tares from this test entry behaved as expected and were very repeatable. The thrust tares were performed at various back pressures in the tunnel in both air and nitrogen operations at both warm and cryogenic temperatures. Figure 15(a) shows the thrust tare results for the balance axial force and it can be seen that different amounts of thrust were generated at the different tunnel back pressures, but the data collapses into a single curve once it is nondimensionalized by the back pressure and reference area (Figure 15(b)). Also, note that repeat thrust tares were performed at the 21.5 and 26.5 psia tunnel back pressures and it is clear that the thrust tare data repeated very well.

For the cruise configuration, the static thrust is measured mostly in balance axial force, but with the slight thrust vector angle in the pitch plane, some of the thrust was measured in balance normal force as well. The geometric thrust vector angles were listed in Table 3, but the effective thrust vector angle could be different due to the Coandă effect of the wall-bounded jet. The balance axial and normal force data from the thrust tare was used to calculate the effective thrust vector angle in the pitch plane according to Equation 8. Figure 16 shows the nondimensional balance AF and NF data as well as the calculated effective thrust

vector angle. The effective angle is close to the geometric thrust vector angle (7 - 8 deg) at higher blowing rates, but is different at the lower blowing rates.

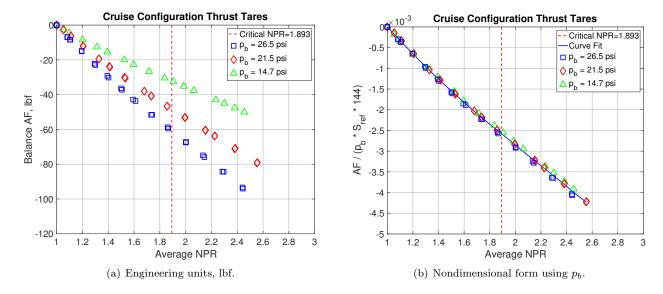


Figure 15. Thrust tare results for balance axial force (AF) in (a) engineering units and (b) nondimensional form.

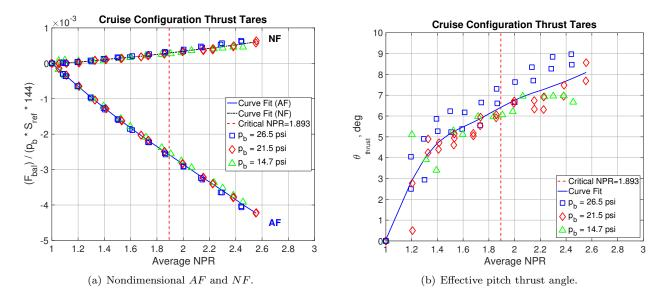


Figure 16. Thrust tare results for balance axial force (AF) and normal force (NF) and calculation of effective thrust angle (θ_{thrust}) .

While the preferred method for thrust removal is to use the balance data, it is also desirable to have the ideal thrust method display similar data trends as verification of the balance results. For the FAST-MAC model, one of the main problems with the ideal thrust method was the calculation of a discharge coefficient. The method of using the ratio of the measured weight flow rate to the ideal weight flow rate did not produce reasonable or physical values (discharge coefficients over 1). Therefore, C_{dis} was always set to 1 in the ideal thrust equations. However, the balance data can be used to estimate the discharge coefficient by comparing the total resultant thrust magnitude from the balance to the calculated total ideal thrust. The NTF-117S balance does not have a side force measurement capability so the resultant thrust magnitude would be missing a component. Instead, the balance axial force was compared to the x-component of the total ideal thrust (Equation 12) and discharge coefficients were calculated as a function of NPR using the ratio between the two data curves as shown in Figure 17. The resulting discharge coefficient values between 0.85 and 0.90

are very reasonable and the trend with NPR was also reasonable. These discharge coefficients were then used to correct the values of the momentum thrust coefficient C_{μ} .

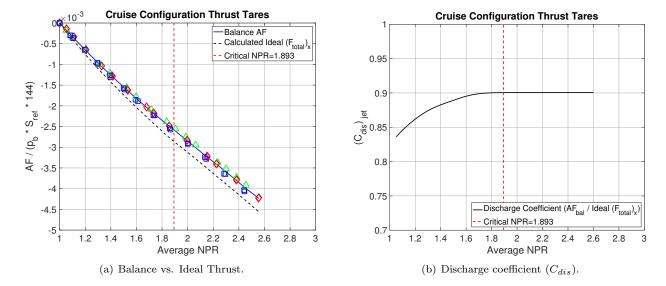


Figure 17. Comparison of thrust tare results between balance AF data and calculated ideal thrust. The discharge coefficient is also calculated from these results.

C. Transonic Results

The results presented in this section will highlight powered increments or decrements due to the wing trailing-edge blowing. The results will be focused on Mach numbers of 0.85 and 0.88 at Reynolds numbers based on mean aerodynamic chord of 15 million and 30 million. The Mach 0.85 condition is the on-design condition for the wing where the flow over the unblown wing is fully attached. The Mach 0.88 condition is an off-design condition where the unblown wing experiences significant shock-induced flow separation.

The tunnel stagnation temperature for the experiment was -50°F for cryogenic mode operations to reach the highest Reynolds numbers and 120°F in air mode operations. Data were acquired at angles of attack between -6° and +6° and the circulation control blowing varied up to NPR values of 2.0 and up to C_{μ} values of 0.006. The results shown are static thrust-removed quantities and the balance data from the thrust tares was used for thrust removal. The increment uncertainty development is based on the data repeatability results and will be used for reference on many of the plots.

1. Wing Surface Pressures

There are four pressure rows on the FAST-MAC model located at semispan locations of 20%, 40%, 60%, and 80% as shown in Figure 18. Analysis of wing surface pressure data from previous test entries for the two outboard pressure rows on the 0° flap cruise configuration showed encouraging results, suggesting the potential for cruise drag reduction as a consequence of the blowing.¹⁹ Similar results were seen in the wing surface pressures from this test entry. Figure 19 shows wing surface pressures for the most outboard pressure row at $\eta=0.8$ at 15 and 30 million Reynolds number for $M_{\infty}=0.85$ and $M_{\infty}=0.88$. The data were acquired at 3 degrees angle of attack corresponding to roughly $C_L=0.6$, at the unblown condition and also two blowing conditions of increasing NPR.

For attached flow conditions at $M_{\infty}=0.85$ and $Re=30\mathrm{M}$, the blowing increased the lift and moved the shockwave slightly aft on the wing, without changing the strength of the shock. However, similar benefits could not be seen at the lower Reynolds number of 15 million for $M_{\infty}=0.85$. At the off-design condition of $M_{\infty}=0.88$ at both $Re=15\mathrm{M}$ and 30M, the blowing was effective in re-attaching the shock-induced flow separation and moved the shockwave aft about 10% chord with no increase in shock strength.

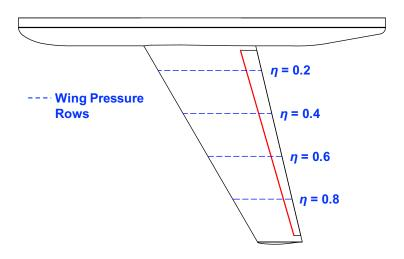


Figure 18. Wing surface pressure rows on the FAST-MAC model.

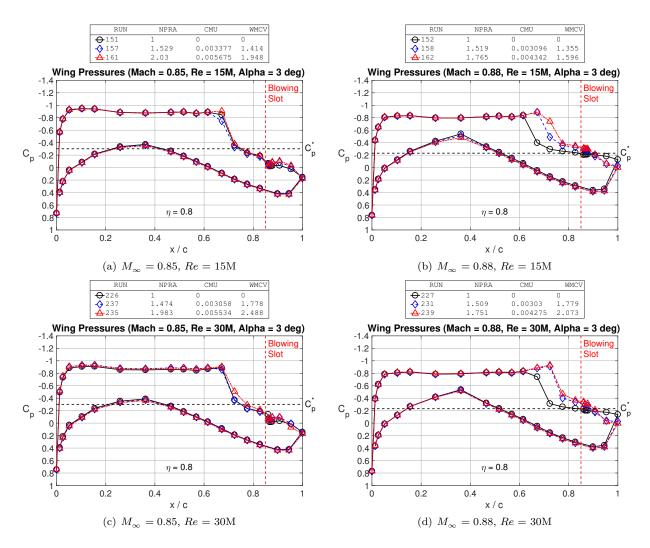


Figure 19. Wing surface pressures for most outboard pressure row ($\eta=0.8$) at 3° angle of attack at Re=15 and 30 million for $M_{\infty}=0.85$ and $M_{\infty}=0.88$.

2. Uncertainty on Increments Due to Blowing

The powered increments or decrements due to wing trailing-edge blowing is the difference between a blowing data set and a non-blowing data set as shown in Equation 13 where X is the parameter of interest such as C_D , C_L , C_m , or M * L/D. Note that the blowing data set also includes removal of the static thrust effect on the parameter of interest.

$$\Delta X_{Blowing} = X_{BlowOn} - X_{NoBlow} \tag{13}$$

To determine the uncertainty on the powered increment, the error propagation equation is shown in Equation 14 where σ_X is the uncertainty associated with the parameter X, k is a coverage factor (typically 2 for 2σ coverage), and ρ is the correlation coefficient between the blowing and non-blowing uncertainty terms.

$$U_{\Delta X_{Blowing}} = \sqrt{\left(k\,\sigma_{X}\right)_{BlowOn}^{2} + \left(k\,\sigma_{X}\right)_{NoBlow}^{2} - 2\,\rho\,\left(k\,\sigma_{X}\right)_{BlowOn}\left(k\,\sigma_{X}\right)_{NoBlow}} \tag{14}$$

The σ_X uncertainty term can be expanded into component terms related to the balance calibration uncertainty $(\sigma_{X_{Balance}})$ and the data repeatability uncertainty $(\sigma_{X_{Repeat}})$. The error propagation equation is then expanded as shown in Equation 15.

$$U_{\Delta X_{Blowing}} = \sqrt{\frac{\left[\left(k\,\sigma_{X}\right)_{Balance}^{2} + \left(k\,\sigma_{X}\right)_{Repeat}^{2}\right]_{BlowOn} + \left[\left(k\,\sigma_{X}\right)_{Balance}^{2} + \left(k\,\sigma_{X}\right)_{Repeat}^{2}\right]_{NoBlow}} - 2\,\rho\,\sqrt{\left[\left(k\,\sigma_{X}\right)_{Balance}^{2} + \left(k\,\sigma_{X}\right)_{Repeat}^{2}\right]_{BlowOn}}\,\sqrt{\left[\left(k\,\sigma_{X}\right)_{Balance}^{2} + \left(k\,\sigma_{X}\right)_{Repeat}^{2}\right]_{NoBlow}}}$$

$$(15)$$

For simplicity, the uncertainty terms between the blowing data and the non-blowing data are assumed to be the same since the same strain gauge balance was used to acquire both data sets and the data repeatability analysis from Section IV-A showed very little difference between a blowing data set and a non-blowing data set. The error propagation equation can then be simplified and rearranged as shown in Equations 16 and 17.

$$U_{\Delta X_{Blowing}} = \sqrt{2 \left[\left(k \, \sigma_X \right)_{Balance}^2 + \left(k \, \sigma_X \right)_{Repeat}^2 \right] - 2 \, \rho \left[\left(k \, \sigma_X \right)_{Balance}^2 + \left(k \, \sigma_X \right)_{Repeat}^2 \right]}$$
(16)

$$U_{\Delta X_{Blowing}} = \sqrt{2 \left[\left(k \, \sigma_X \right)_{Balance}^2 - \rho_{Balance} \, \left(k \, \sigma_X \right)_{Balance}^2 + \left(k \, \sigma_X \right)_{Repeat}^2 - \rho_{Repeat} \, \left(k \, \sigma_X \right)_{Repeat}^2 \right]}$$
(17)

Furthermore, it is assumed that the balance uncertainty term is fully correlated ($\rho_{Balance}=1$) between a blowing and a non-blowing data set since the same balance was used and the measurement levels would be at similar points on the balance calibration curve. The repeatability uncertainty term is assumed to be a random error source so there would be no correlation ($\rho_{Repeat}=0$) between a blowing and non-blowing data set. Applying the correlation coefficients cancels out the balance calibration uncertainty term and what is left is the repeatability uncertainty term with a $\sqrt{2}$ factor as shown in Equations 18 to 20. This uncertainty with a coverage factor (k) of 2 will be used on the powered increments shown in the results presented in subsequent sections.

$$U_{\Delta X_{Blowing}} = \sqrt{2 \left[\left(k \, \sigma_X \right)_{Balance}^2 - \rho_{Balance} \left(k \, \sigma_X \right)_{Balance}^2 + \left(k \, \sigma_X \right)_{Repeat}^2 - \rho_{Repeat} \left(k \, \sigma_X \right)_{Repeat}^2 \right]}$$
(18)

$$U_{\Delta X_{Blowing}} = \sqrt{2 \left(k \, \sigma_X\right)_{Repeat}^2} \tag{19}$$

$$U_{\Delta X_{Blowing}} = 1.414 \left(2 \,\sigma_X\right)_{Repeat} \tag{20}$$

3. Lift Increments Due to Blowing

Figure 20 shows the thrust-removed corrected lift coefficient and powered lift increment (ΔC_L) data for $M_{\infty}=0.85$ and $M_{\infty}=0.88$ at 30 million chord Reynolds number. The uncertainty on the lift increment developed earlier is shown on the plots for reference. At $M_{\infty}=0.85$, the blowing provided a noticeable increase in the lift coefficient across the angle-of-attack range at the highest blowing rate at NPR=2, but only showed a lift increase at the higher angles of attack for the blowing data at NPR=1.5. As will be shown in a later section, at the on-design condition of $M_{\infty}=0.85$, a loss of lift occurs at low blowing rates and doesn't return to the unpowered lift level until a higher blowing rate of about NPR=1.5. At $M_{\infty}=0.88$, the data showed an increase in the lift coefficient across most of the angle-of-attack range for both blowing rates tested, corroborating the surface pressure analysis from the previous test that showed the shockwave was moved aft without changing the shock strength. Although the data at 15 million chord Reynolds number is not shown, similar lift increment results were seen at that condition.

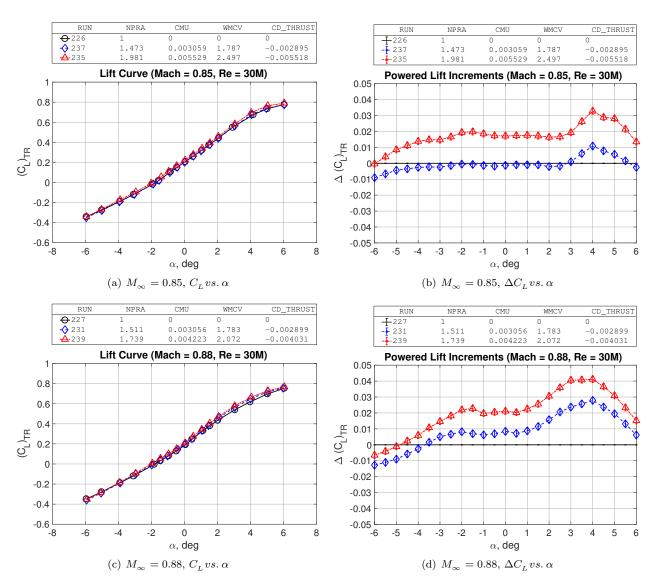


Figure 20. Thrust-removed corrected lift coefficient data and powered lift increments at Re= 30 million for $M_{\infty}=0.85$ and $M_{\infty}=0.88$.

4. Drag Decrements Due to Blowing

To investigate whether the circulation control blowing provided an overall drag reduction, the thrust-removed C_D data were evaluated at constant C_L values by linearly interpolating each $log_{10}(C_D)$ data curve as a function of C_L^2 . The interpolation was performed this way due to the linear relationship between C_D and C_L^2 as shown in Figure 21 with C_D plotted on a log scale to better display this linear relationship. The focus of the drag increment results is at $C_L = 0.5$, which is the design lift coefficient of the unblown wing.

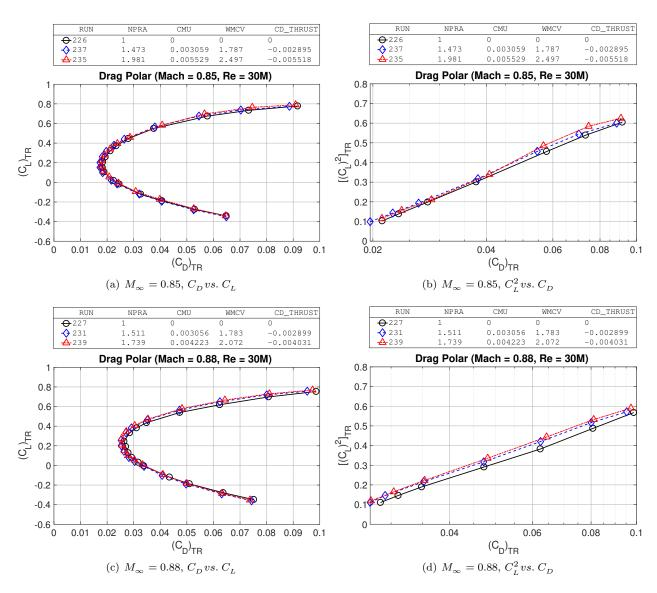


Figure 21. Drag polar at Re= 30 million for $M_{\infty}=0.85$ and $M_{\infty}=0.88$ with linear interpolation of C_D as a function of C_I^2 .

Figure 22 shows the drag increment results at $C_L=0.5$ for $M_\infty=0.85$ and $M_\infty=0.88$ at 15 and 30 million chord Reynolds number. Note that the uncertainty on the drag coefficient increment is ± 4.8 counts. At $M_\infty=0.85$ and $Re=15\mathrm{M}$, the blowing resulted in an overall drag increase of about 10 counts at NPR=1.5. However, at $M_\infty=0.85$ and $Re=30\mathrm{M}$, the blowing resulted in an overall drag decrease of about 12 counts at NPR=1.5. In both cases, the higher blowing rate of NPR=2 resulted in a direction reversal in the drag increment as compared to the NPR=1.5 data. This result is curious and contradicts the trend seen in the past with increased blowing rates. However, for this on-design condition, it is easy to adversely affect the optimized wing aerodynamics with the introduction of blowing, but the results show that there are some drag reduction benefits if the blowing rate is high enough. For the off-design condition

at $M_{\infty}=0.88$, even a small amount of blowing can help to combat the shock-induced flow separation and re-attach the flow. At the $Re=15\mathrm{M}$ condition, a significant drag reduction of 24 counts at $C_{L}=0.5$ was realized and an even greater drag reduction of 37 counts was seen at the $Re=30\mathrm{M}$ condition.

The drag increments for other constant positive lift coefficients are shown in Figure 23 and the ± 4.8 counts increment uncertainty is shown on each data curve for reference. At the $Re=30\mathrm{M}$ condition, there was an overall drag reduction across the lift coefficients of interest for all blowing rates tested and at both Mach numbers tested, even at the on-design condition of $M_{\infty}=0.85$. The drag reduction benefit increases for higher lift coefficients corresponding to higher angles of attack since the blowing is able to counteract some of the flow separation occurring at the higher angles of attack. These results also demonstrate the importance of testing at relevant flight Reynolds numbers since the benefits seen at $M_{\infty}=0.85$ were not entirely present at the lower $Re=15\mathrm{M}$ condition, but were clear at $Re=30\mathrm{M}$.

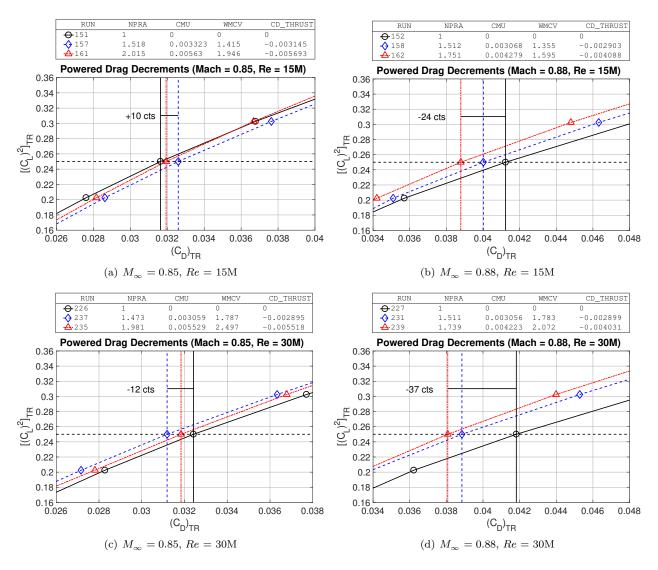


Figure 22. Thrust-removed drag increments at $C_L=0.5$ due to the induced effect of the circulation control blowing at Re=15 and 30 million for $M_\infty=0.85$ and $M_\infty=0.88$.

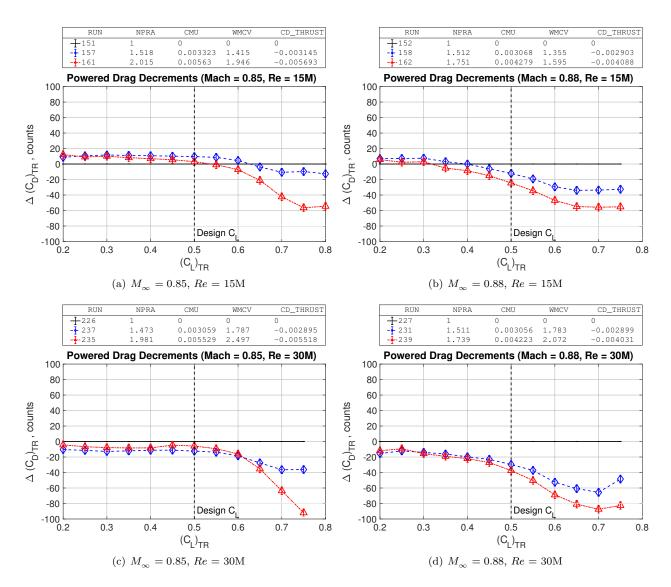


Figure 23. Thrust-removed drag increments at constant lift coefficients at Re= 15 and 30 million for $M_{\infty}=0.85$ and $M_{\infty}=0.88$.

A few NPR sweep runs at a constant 3° angle of attack corresponding to roughly $C_L=0.6$ were acquired at $M_\infty=0.85$ and $M_\infty=0.88$. Two examples are shown in Figure 24. For the sweeps, an unpowered data point was first acquired, then data points at increasing NPR and C_μ values were acquired. In the plots, the lift-induced drag component is removed from the drag coefficient data to better visualize the overall drag reduction benefit from the blowing. As mentioned earlier, blowing at low NPR rates at $M_\infty=0.85$ spoiled the lift on the configuration until about NPR=1.5 when the lift coefficient recovered to the same level as the unpowered data point and the drag coefficient was reduced by 6 counts. At $M_\infty=0.88$, it didn't take much blowing to recover to the same lift coefficient as the unpowered point. At about NPR=1.2, the lift coefficient recovered, but with a 19 count reduction in drag coefficient. A NPR sweep at $Re=30\mathrm{M}$ was not acquired for $M_\infty=0.88$, but the drag reduction benefits would be expected to be better. These results suggest that at off-design conditions, even a small amount of blowing can improve the flow over the trailing edge of the wing and provide a drag reduction benefit. However, at the design condition, a small amount of blowing can disrupt the performance of the wing and a large amount of blowing is required to achieve any benefit.

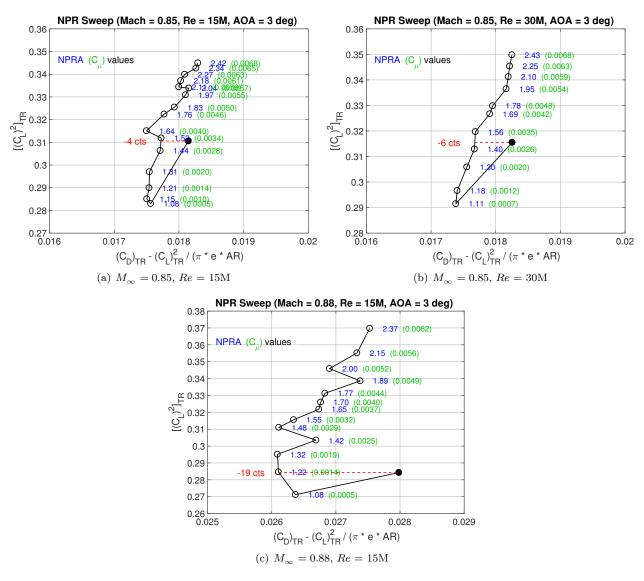


Figure 24. Thrust-removed NPR sweeps at constant 3° angle of attack at Re=15 and 30 million for $M_{\infty}=0.85$ and Re=15 million for $M_{\infty}=0.88$. Average NPR values shown in blue and C_{μ} values shown in green for each data point.

5. Aerodynamic Efficiency Increments Due to Blowing

The lift and drag increments due to blowing were presented earlier and with the increased lift and reduced drag seen in the data, it follows that the overall aerodynamic efficiency (M*L/D) of the configuration would increase as a result of the blowing. This is shown in Figure 25 at $Re=30\mathrm{M}$ for both $M_{\infty}=0.85$ and $M_{\infty}=0.88$. The increments showed an increase in aerodynamic efficiency across the lift coefficients of interest and at the design lift coefficient of $C_L=0.5$, the data showed a $\Delta(M*L/D)=0.5$ at $M_{\infty}=0.85$ and a $\Delta(M*L/D)=1.0$ at $M_{\infty}=0.88$, which are significant increases to overall aerodynamic efficiency.

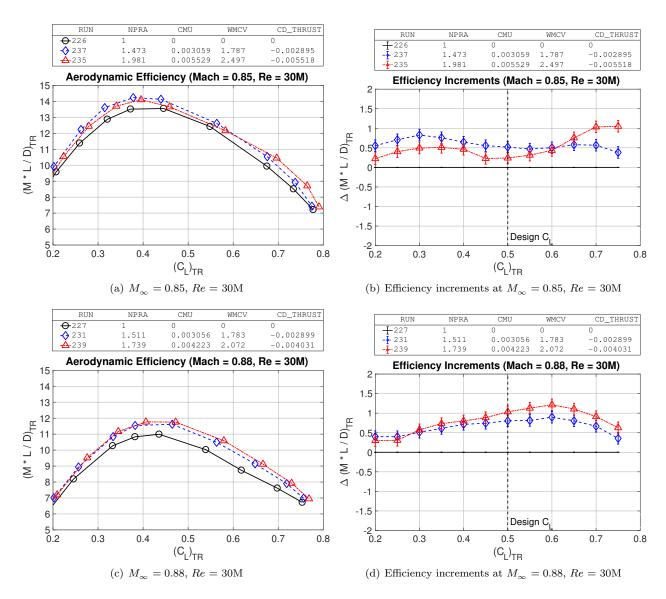


Figure 25. Thrust-removed aerodynamic efficiency increments at Re=30 million for $M_{\infty}=0.85$ and $M_{\infty}=0.88$.

V. Concluding Remarks

The focus of this paper has been on evaluating the induced effects of wing trailing-edge blowing on the transonic aerodynamics for the FAST-MAC circulation control model that was tested for the third time at the National Transonic Facility. The model allowed independent control of four circulation control plenums producing a high momentum jet from a blowing slot near the wing trailing edge that was directed over a 15% chord simple-hinged flap. The experiment was designed to determine the potential for transonic drag reduction with the circulation control blowing. Recent upgrades to transonic semispan flow control testing at the NTF have demonstrated an improvement to overall data repeatability that allows for increased confidence in the data results.

The results were focused on Mach numbers of 0.85 and 0.88 at Reynolds numbers based on mean aerodynamic chord of 15 million and 30 million. An evaluation of two methods for static thrust removal was performed and the static thrust generated by the blowing slot was removed from the wind-on data using force and moment balance data from wind-off thrust tares. The thrust-removed corrected data results with uncertainty bounds showed that an overall drag reduction and increased aerodynamic efficiency was realized as a consequence of the blowing for both Mach numbers especially at the flight Reynolds numbers of 30 million. Table 4 summarizes the C_L , C_D , and M*L/D increments due to blowing at the design $C_L=0.5$.

Table 4. Summary of C_L , C_D , and M*L/D increments due to blowing at $C_L=0.5$.

	$M_{\infty} = 0.85$		$M_{\infty} = 0.88$		
Increment	Re = 15M	Re = 30M	Re = 15M	Re = 30M	Uncertainty
$\Delta C_{\scriptscriptstyle L}$	0.02	0.017	0.036	0.036	± 0.002
$\Delta C_{\scriptscriptstyle D}$	10 cts	-12 cts	-24 cts	-37 cts	$\pm 4.8 \mathrm{~cts}$
$\Delta(M*L/D)$	-0.4	0.5	0.7	1.0	± 0.15

A fourth FAST-MAC experiment is underway to evaluate the performance of fluidic or sweeping jet actuators against the steady blowing performance described in this paper. The goal of that experiment is to determine whether similar performance benefits can be achieved with the sweeping jet actuators, but at a significantly reduced total weight flow rate.

Acknowledgements

The research has been supported by the Advanced Air Transport Technology project within the NASA Advanced Air Vehicles Program. Special thanks are given to Richard Wahls, Susan Wilz, Scott Anders, Sally Viken, and Zac Applin for their continued support and encouragement. The successful third test of the FAST-MAC model could not have been accomplished without the dedication, technical expertise, and energy of the entire staff at the National Transonic Facility.

References

¹Zeune, C. H., "An Overview of the Air Force's Speed Agile Concept Demonstration Program," AIAA Paper 2013-1097, AIAA, January 2013.

²Barberie, F. J., Wick, A. T., Hooker, J. R., and Zeune, C. H., "Low Speed Powered Lift Testing of a Transonic Cruise Efficient STOL Military Transport," AIAA Paper 2013-1099, AIAA, January 2013.

³Hooker, J. R., Wick, A. T., Zeune, C. H., Jones, G. S., and Milholen-II, W. E., "Design and Transonic Wind Tunnel Testing of a Cruise Efficient STOL Military Transport," AIAA Paper 2013-1100, AIAA, January 2013.

⁴Harrison, N. A., Vassberg, J. C., DeHaan, M. A., and Gea, L.-M., "The Design and Test of a Swept Wing Upper Surface Blowing (USB) Concept," AIAA Paper 2013-1102, AIAA, January 2013.

⁵Collins, S. W., Westra, B. W., Lin, J. C., Jones, G. S., and Zeune, C. H., "Wind Tunnel Testing of Powered Lift, All-Wing STOL Model," RAeS 566-5A3, Royal Aeronautical Society, London, July 2008.

⁶Jameson, K. K., Marshall, D. D., Ehrmann, R., Lichtwardt, J. A., Paciano, E., Englar, R. J., and Horne, W. C., "Cal Poly's AMELIA 10 Foot Span Hybrid Wing-Body Low Noise CESTOL Aircraft Wind Tunnel Test and Experimental Results Overview," AIAA Paper 2013-0974, AIAA, January 2013.

⁷Jones, G. S., Lin, J. C., Allan, B. G., Milholen-II, W. E., Rumsey, C. L., and Swanson, R. C., "Overview of CFD Validation Experiments for Circulation Control Applications at NASA," RAeS 566-8A1, Royal Aeronautical Society, London, July 2008

⁸Wick, A. T., Hooker, J. R., Barberie, F. J., and Zeune, C. H., "Powered Lift CFD Predictions of a Transonic Cruising STOL Military Transport," AIAA Paper 2013-1098, AIAA, January 2013.

⁹Marshall, D. D., Lichtwardt, J. A., Pham, J., Blessing, B., and Storm, T. M., "Summary of the Aerodynamic Modeling Efforts for AMELIA," AIAA Paper 2013-0973, AIAA, January 2013.

¹⁰Englar, R. J., Jones, G. S., Allan, B. G., and Lin, J. C., "2-D Circulation Control Airfoil Benchmark Experiments Intended for CFD Code Validation," AIAA Paper 2009-902, AIAA, January 2009.

¹¹Pfingsten, K. C. and Radespiel, R., "Experimental and Numerical Investigation of a Circulation Control Airfoil," AIAA Paper 2009-533, AIAA, January 2009.

¹²Swanson, R. C., Rumsey, C. L., and Anders, S. G., "Progress Towards Computational Method for Circulation Control Airfoils," AIAA Paper 2005-89, AIAA, January 2005.

¹³Rogers, E. O. and Donnelly, M. J., "Characteristics of a Dual-Slotted Circulation Control Wing of Low Aspect Ratio Intended for Naval Hydrodynamic Applications," AIAA Paper 2004-1244, AIAA, January 2004.

¹⁴Jones, G. S., Viken, S. A., Washburn, A. E., Jenkins, L. N., and Cagle, C. M., "An Active Flow Circulation Controlled Flap Concept for General Aviation Aircraft Applications," AIAA Paper 2002-3157, AIAA, June 2002.

¹⁵ Alexander, M. G., Anders, S. G., Johnson, S. K., Florance, J. P., and Keller, D. F., "Trailing Edge Blowing on a Two-Dimensional Six-Percent Thick Elliptical Circulation Control Airfoil Up to Transonic Conditions," NASA TM 2005-213545, NASA Langley Research Center, March 2005.

¹⁶Milholen-II, W. E., Jones, G. S., Chan, D. T., and Goodliff, S. L., "High-Reynolds Number Circulation Control Testing in the National Transonic Facility (Invited)," AIAA Paper 2012-0103, AIAA, January 2012.

- ¹⁷Englar, R. J., "Two-Dimensional Transonic Wind Tunnel Tests of Three 15-Percent-Thick Circulation Control Airfoils," Technical Note AL-182, AD 882-075, Naval Ship Research and Development Center, December 1970.
- ¹⁸Schlecht, R. and Anders, S. G., "Parametric Evaluation of Thin, Transonic Circulation Control Airfoils," AIAA Paper 2007-272, AIAA, January 2007.
- ¹⁹Milholen-II, W. E., Jones, G. S., Chan, D. T., Goodliff, S. L., Anders, S. G., Melton, L. P., Carter, M. B., Allan, B. G., and Capone, F. J., "Enhancements to the FAST-MAC Circulation Control Model and Recent High-Reynolds Number Testing in the National Transonic Facility," AIAA Paper 2013-2794, AIAA, June 2013.
 - $^{20} http://www.aeronautics.nasa.gov/aavp/aetc/transonic/ntf.html, "National Transonic Facility (NTF)," \ .$
 - ²¹NTF, "NTF User Guide," NASA Document SP-2011-5-110-LaRC, NASA Langley Research Center, February 2012.
- ²²Wahls, R. A., "The National Transonic Facility: A Research Retrospective (Invited)," AIAA Paper 2001-754, AIAA, January 2001.
- ²³Goodliff, S. L., Jones, G. S., Balakrishna, S., Chan, D. T., Milholen-II, W. E., Butler, D., and Cagle, C. M., "Force Measurement Improvements to the National Transonic Facility Sidewall Model Support System," AIAA Paper 2016-0648, AIAA, January 2016.
- ²⁴Lynn, K. C., Toro, K. G., Chan, D. T., Balakrishna, S., and Landman, D., "Enhancements to the National Transonic Facility High-Reynolds Number Active Blowing Semi-Span Force Measurement System," *Journal of Aircraft*, Vol. 52, No. 6, November 2015, pp. 1736–1755.
- ²⁵Paryz, R. W., "Subsonic Transonic Applied Refinements By Using Key Strategies STARBUKS In the NASA Langley Research Center National Transonic Facility," AIAA Paper 2014-1481, AIAA, January 2014.
- ²⁶Chan, D. T., Balakrishna, S., Walker, E. L., and Goodliff, S. L., "Mach Stability Improvements Using an Existing Second Throat Capability at the National Transonic Facility (Invited)," AIAA Paper 2015-0622, AIAA, January 2015.
- ²⁷Milholen-II, W. E., Jones, G. S., and Cagle, C. M., "NASA High-Reynolds Number Circulation Control Research Overview of CFD and Planned Experiments (Invited)," AIAA Paper 2010-344, AIAA, January 2010.
- ²⁸Englar, R. J., Smith, M. J., Kelley, S. M., and Rover-III, R. C., "Application of Circulation Control Technology to Advanced Subsonic Transport Aircraft, Part I: Airfoil Development," *Journal of Aircraft*, Vol. 31, No. 5, Sept-Oct 1994, pp. 1160–1168.
- ²⁹Gatlin, G. M., Parker, P. A., and Owens, L. R., "Development of a Semi-Span Test Capability at the National Transonic Facility," AIAA Paper 2001-0759, AIAA, January 2001.
- ³⁰Jones, G. S., Milholen-II, W. E., Chan, D. T., Allan, B., Goodliff, S. L., Melton, L., Anders, S. G., Carter, M., and Capone, F., "Development of the Circulation Control Flow Scheme used in the NTF Semi-Span FAST-MAC Model," AIAA Paper 2013-3048, AIAA, June 2013.
 - ³¹Lynn, K. C., "Development of the NTF-117S Semi-Span Balance," AIAA Paper 2010-4542, AIAA, June 2010.
 - ³²Wheeler, D. and Chambers, D., Understanding Statistical Process Control, SPC Press, Knoxville, 2nd ed., 1992.
 - ³³Montgomery, D. C., Introduction to Statistical Quality Control, John Wiley and Sons, Inc., New York, 5th ed., 2005.
- ³⁴Chan, D. T., Milholen-II, W. E., Jones, G. S., and Goodliff, S. L., "Thrust Removal Methodology for the FAST-MAC Circulation Control Model Tested in the National Transonic Facility," AIAA Paper 2014-2402, AIAA, June 2014.